Journal of the European Ceramic Society 45 (2025) 116812

Contents lists available at ScienceDirect

Journal of the European Ceramic Society

journal homepage: www.elsevier.com/locate/jeurceramsoc

Photolithographic additive manufacturing of high-entropy perovskite oxides from synthesized multimetallic polymeric precursors

Haotian Yang [a,*,1], Xifan Wang [a], Sebastian Praetz [b,2], Shumin Pang [a,3], Oliver Görke [a], Maged F. Bekheet [a,4], Dorian A.H. Hanaor [a,5], Aleksander Gurlo [a,*,6]

[a] Technische Universität Berlin, Faculty III Process Sciences, Institute of Materials Science and Technology, Chair of Advanced Ceramic Materials, Straße des 17. Juni 135, Berlin 10623, Germany

[b] Technische Universität Berlin, Faculty II - Mathematics and Natural Sciences, Institute for Optics and Atomic Physics, Straße des 17. Juni 135, Berlin 10623, Germany

ARTICLE INFO

Keywords:
Organic-inorganic hybrid resin
Additive manufacturing
High-entropy materials
Perovskite-type oxides
DLP fabrication

ABSTRACT

In this work, the synthesis of high-entropy perovskite-type oxides from multimetallic polymeric precursors and their shaping by photolithographic additive manufacturing is investigated. Thermosets with well-controlled complex geometries are produced by digital light processing using the multimetallic organic-inorganic hybrid resin developed in this work and converted into ceramics by thermal debinding and sintering. The high-entropy perovskite-type oxides are produced at 1500 °C, they retain the printed geometry with high shape fidelity. The orthorhombic crystal structure is identified by the Rietveld refinement of high-resolution synchrotron X-ray data; elemental and spectroscopic characterizations suggest the composition $Sr(Ti_{0.22}Zr_{0.22}Hf_{0.23}Mn_{0.15}Sn_{0.18})O_{2.85}$. The use of aqueous polyethylene glycol as a binder and porogen greatly reduces the formation of cracks and creates evenly distributed micropores, which leads to improved compressive strength of the specimens. The compressive strength of 0.94 MPa is highest for materials printed from the resins with 3 wt% PEG in the woodpile-like geometries.

1. Introduction

High-entropy ceramics, a new class of materials, have emerged as a hotspot of research activities in recent years. Highly entropic ceramics can be described as single-phase proportional solid solutions. They are characterized by a cation sublattice in which at least five different types of cations are evenly and randomly distributed. Research on high-entropy ceramics began in 2015, when Rost et al. reported the preparation of a high-entropy oxide with a rock salt structure[1]. Since then, more and more high-entropy ceramics, including oxides[2–4], borides [5], and carbides[6,7], have been synthesized and studied, opening up various new avenues for the design of functional materials. The high entropy effect caused by multiple components can effectively improve the thermodynamic stability of the material, promote the formation of a single crystal phase, and at the same time provide tunable mechanical[8,9], magnetic, thermoelectric[10], and catalytic properties[11,12].

Among high-entropy ceramics, high-entropy perovskite oxides (HEPOs) are a particularly interesting system. Perovskites are ternary oxides of the form ABO_3 and are known to be effective functional materials for a number of valuable target applications, including ferroelectrics[13], catalysis[14], photovoltaics[15], photocatalysis[16], dielectrics[17], and battery materials[18]. The functionality and versatility of perovskite oxides are due to the structural and chemical flexibility resulting from the various possible cation combinations in the

* Corresponding authors.
E-mail addresses: haotian.yang@ceramics.tu-berlin.de (H. Yang), Xifan828@gmail.com (X. Wang), sebastian.praetz@tu-berli.de (S. Praetz), shumin.Pang@ceramics.tu-berlin.de (S. Pang), oliver.Goerke@ceramics.tu-berlin.de (O. Görke), maged.Bekheet@ceramics.tu-berlin.de (M.F. Bekheet), dorian.Hanaor@ceramics.tu-berlin.de (D.A.H. Hanaor), gurlo@ceramics.tu-berlin.de (A. Gurlo).
[1] ORCID: 0009-0004-7708-4684
[2] ORCID: 0000-0001-6852-7616
[3] ORCID: 0000-0001-6677-121X
[4] ORCID: 0000-0003-1778-0288
[5] ORCID: 0000-0003-4455-7006
[6] ORCID: 0000-0001-7047-666X

https://doi.org/10.1016/j.jeurceramsoc.2024.116812
Received 16 May 2024; Received in revised form 31 July 2024; Accepted 5 August 2024
Available online 6 August 2024

two cation sublattices. Since B-site sublattices are usually responsible for ferroelectric, magnetic, and transport properties in perovskite systems, the design of B-site occupation, in particular, is seen as an effective approach for tailoring the properties of these materials[19]. Populating this site with five or more elements offers ways to achieve further functional tunability or unexpected physical phenomena. Criteria for the formation of HEPO phases based on structural tolerance [3] and valence differences [20] have been proposed. The multi-element occupation of the B-site and the resulting high configurational entropy endow HEPOs with interesting functional properties, including ultra-low thermal conductivity[21], low dielectric loss[22], superior cycle and rate performance as lithium-ion battery anode[23], and catalytic activity towards oxygen and hydrogen evolution[24,25]. A representative example is perovskite-type $SrTiO_3$. Among the numerous known perovskite-type oxides, $SrTiO_3$ is widely used for photocatalytic hydrogen generation and photocatalytic degradation due to its high photocatalytic activity[26–28]. However, the photocatalytic reaction with this material must be carried out under ultraviolet light due to the wide band gap (3.2 eV) of $SrTiO_3$[29,30]. Doping at the B-site is a widely used and effective strategy to reduce the band gap of $SrTiO_3$[31–33]. Therefore, the B-site high-entropy perovskite oxide is expected to have a narrower band gap and achieve more efficient photocatalysis under visible light.

Previous reports on high-entropy ceramics have focused on the compositional predictions, the development of synthesis processes, and the characterization of various properties. In most of the studies conducted to date, binary metal oxides are usually used as starting materials for the synthesis of HEPOs. Since high-entropy ceramics contain a variety of randomly distributed metal cations, the dispersion of the elements poses a major challenge in the formation of homogeneous materials. Vigorous grinding is generally required to disperse the various components in solid-state methods, and extremely high heat-treatment temperatures are needed to accelerate the diffusion of constituents[34,35]. In solid-state methods the high formation temperature will lead to grain coarsening, and the ball milling will inevitably introduce impurities. What is more, the shaping and processing of high-entropy ceramics are limited by the typical powder-based routes.

The manufacture of ceramics most commonly relies on the use of molds, and the shapes of ceramic parts are limited to relatively simple geometries. The machining of complex shapes is further hindered by the high hardness and brittleness of ceramic materials. Additive manufacturing technologies provide new pathways to produce materials, including ceramics, in complex forms and shapes. The ability to additively manufacture materials opens up possibilities for the design and implementation of functional ceramics in high-value applications. Digital Light Processing (DLP) is a vat-polymerization printing approach, considered to be a type of photolithography, widely used in the production of advanced materials with fine features and high geometric complexity[36,37]. In this approach, light is projected, most commonly via a mirror, onto the surface of a photopolymerizable resin, bringing about its area selective hardening in a layer-by-layer manner. This method can be applied towards the forming of ceramics when polymerizable preceramic polymers are used as precursors. However, this type of additive manufacturing of ceramics faces several challenges. During the thermal debinding and/or decomposition of polymeric precursors to ceramics the evolution of gaseous species, significant weight loss, and capillary forces cause extensive shrinkage, leading to catastrophic cracking of ceramics[38,39]. Liquid-based additive manufacturing of ceramics has mainly concentrated on silicon-containing polymer-derived ceramics[40–42]. To reduce the shrinkage and cracking of ceramic fabricated from the liquid precursors, another approach involves stereolithographic 3D printing of ceramic materials from resins with dispersed ceramic particles. However, this approach is encumbered by light scattering by particles and is naturally quite limited with regard to the range of geometries and ceramic materials that can be manufactured. The majority of ceramics, including TiO_2, $SrTiO_3$, and other perovskites, are particularly challenging to process via such routes owing to their high refractive index[43]. A further emerging technology in the additive manufacturing of ceramics is two-photon lithography, which provides extremely high printing accuracy but is limited to microgeometries[44,45].

Here we propose a novel additive manufacturing method for fabricating high-entropy perovskite oxides from liquid precursors. By using wet chemical synthesis methods, multiple cations can be evenly dispersed in the solution, and molecular-level homogeneous precursors can be easily obtained, which leads to lower formation temperature and finer grain of high-entropy ceramics[46]. Hybrid resins composed of a multimetallic polymeric precursor and photopolymers are printed by DLP, with the high-entropy phase formed through pyrolysis and sintering at ambient pressure. As a binder and porogen, polyethylene glycol is shown to greatly reduce cracks and create uniformly distributed micron pores in the final ceramic body, lending to improved compressive strength. This is the first time that the additive manufacturing of high-entropy ceramics has been realized, further broadening the toolset of ceramic additive manufacturing. For this case study, we selected the targeted composition $Sr(Ti_{0.2}Zr_{0.2}Hf_{0.2}Mn_{0.2}Sn_{0.2})O_3$ in which strontium cations (Sr^{2+}) occupy the A-site, while five other cations (Ti^{4+}, Zr^{4+}, Hf^{4+}, Mn^{4+}, Sn^{4+}) in equal proportions occupy the B-site of the perovskite-type structure.

Table 1
Compositions of the photocurable hybrid resins used for DLP fabrication.

Abbreviation	Precursor[a]/ g	AA[b]/ g	GDD[c]/ g	TPO-L[d]/g	PEG[e]/ g	Water/ g
PEG−0	10	1.5	1	0.25	-	1
PEG−1	10	1.5	1	0.25	0.1	0.9
PEG−2	10	1.5	1	0.25	0.2	0.8
PEG−3	10	1.5	1	0.25	0.3	0.7

[a] Multimetallic polymeric precursor.
[b] Acrylic acid.
[c] Glycerol 1,3-diglycerolate diacrylate.
[d] Ethyl (2,4,6-trimethylbenzoyl) phenylphosphinate.
[e] Polyethylene glycol.

2. Materials and methods

2.1. Synthesis of polymeric precursor

Following our molecular synthesis approach towards high entropy ceramics [47], in this work we aim to synthesize a high-entropy perovskite-type oxide with the targeted composition $Sr(Ti_{0.2}Zr_{0.2}Hf_{0.2}Mn_{0.2}Sn_{0.2})O_3$ in which strontium cations (Sr^{2+}) occupy the A-site, while five other cations (Ti^{4+}, Zr^{4+}, Hf^{4+}, Mn^{4+}, Sn^{4+}) in equal proportions occupy the B-site of the perovskite-type structure. For the precursor synthesis, metal chlorides, $SrCl_2 \times 6\ H_2O$ (11.11 g, 99 %, Merck, Germany), $TiCl_4$ (0.91 ml, 99.9 %, Sigma-Aldrich, Germany), $ZrOCl_2 \times 8\ H_2O$ (2.69 g, 98 %, Sigma-Aldrich, Germany), $HfOCl_2 \times 8\ H_2O$ (3.41 g, 98 %, Alfa Aesar, Germany), $SnCl_4 \times 5\ H_2O$ (2.92 g, 98 %, Alfa Aesar, Germany), and $MnCl_2 \times 4\ H_2O$ (1.65 g, 99 %, Chemsolute, Germany) taken in a molar ratio of 5:1:1:1:1:1, respectively, were dissolved in 13.98 ml ethylene glycol (anhydrous, 99.8 %, Sigma-Aldrich, Germany) with a molar ratio of cations to EG equal to 1:3 and stirred at 80 °C for 1 hour. The solution was dried at 40 °C for 30 min under vacuum to remove excess water and HCl resulting in a multimetallic polymeric precursor (hereinafter referred to as "precursor").

2.2. Preparation of photocurable resins for printing

The photocurable hybrid resin for DLP fabrication (“printing”) was prepared by mixing the precursor with acrylic acid (AA, 99 %, Sigma-Aldrich, Germany), glycerol 1,3-diglycerolate diacrylate (GDD, 99 %, Sigma-Aldrich, Germany), ethyl (2,4,6-trimethylbenzoyl)

phenylphosphinate (TPO-L, Rahn, Germany), and Sudan Orange G (85 %, Sigma-Aldrich, Germany). TPO-L was used as a photoinitiator due to its good solubility and partial compatibility with our light source; Sudan Orange G was used as a photon absorber to reduce light penetration depth and thus control printing accuracy. Table 1 provides an overview of the sample compositions studied in this work. To reduce the cracks in the final ceramic monoliths, polyethylene glycol (PEG, M_w=20000, Merck, Germany) was used as a binder and porogen. The influence of PEG on crack elimination and mechanical properties was investigated by producing four samples with the weight ratio PEG: precursor = 0: 10; 0.1: 10, 0.2: 10, and 0.3: 10 by mixing the photopolymerizable resin containing 10 g precursor with 1 g of aqueous solution with 0, 10, 20, and 30 wt% PEG, respectively, followed by stirring for 1 h.

2.3. Digital light processing

Digital Light Processing of the hybrid resins was carried on a benchtop printer (LittleRP2, LittleRP, USA) with an MC. JLE11.001 UHP lamp of an Acer X152H projector as the light source as described in our previous work[48]. Each layer was printed with a thickness of 0.1 mm with an exposure time of 40 s. The printed rubber-like samples (hereinafter referred to as "printed thermosets") were washed with isopropanol (98 %, VWR chemicals) to remove residual resin from the surface and dried in an oven in air at 170 °C for 24 h to evaporate the excess solvent.

2.4. Thermal treatment: debinding and sintering

Thermal debinding (pyrolysis) of the thermosets was conducted in a tube furnace under argon flow at 500 °C for 1 h with a heating rate of 0.3 °C/min and then cooled naturally to room temperature in the furnace. The debinded (pyrolyzed) samples were subsequently sintered in a furnace in ambient air at 1300, 1400, and 1500 °C for 1 hour, with a heating rate of 5 °C/min, and then cooled naturally to room temperature in the furnace. The specimens sintered at 1500 °C are referred hereinafter to as PEG-0–1500, PEG-1–1500, PEG-2–1500, and PEG-3–1500.

2.5. Characterization methods

The optical absorption of the precursors, photon absorber, and photoinitiator was determined in the range between 250 and 800 nm by Ultraviolet-Visible spectroscopy (UV-Vis) in the UV–vis–spectrometer (PerkinElmer Lambda 900, USA) operated in transmission mode. The molecular structures and compositions of the specimens were elucidated by Fourier transform infrared spectroscopy (FTIR, Bruker VERTEX 70, USA) in attenuated total reflection mode from 4000 cm^{-1} to 550 cm^{-1}. The rheological characterization of photocurable resin for printing was carried out on a rotational rheometer (AntonPaar, Physics MCR 301, Austria) equipped with a 2 ° steel cone plate (25 mm diameter) at 25 °C. A shear rate sweep was conducted from 10^{-2} to 3×10^2 s^{-1}. The pyrolysis process of the printed thermosets was investigated by simultaneous thermal analysis (STA, Netzsch STA 409 PC LUXX, Germany) coupled with a mass spectrometer (OMNiStar GSD 320, Germany) from room temperature to 800 °C with a heating rate of 10 °C/min in argon and air. The metal content was determined by inductively coupled plasma optical emission spectroscopy (ICP-OES) in a Horiba Scientific ICP Ultima2 (Horiba, Japan). Powder samples were digested in a mixed aqueous solution of HNO_3 and HF at 220 °C for 5 h in an autoclave. The oxygen content of the materials was measured by ONH836 Elemental Analyzer (LECO Corporation, USA). The weighted samples were heated in an impulse furnace so that the oxygen in the sample reacted with the graphite to produce CO and CO_2, which were quantitatively measured by a non-dispersive infrared cell. A test run was performed through a standard sample before measurement, and each result was averaged over three tests. The phase composition of specimens was examined by X-ray Diffraction (XRD) in a Bruker D8 Diffractometer (Bruker, USA) at 35 kV and 40 mA using Cu-Kα radiation (λ = 1.5406 Å). 2θ value ranging from 15 to 90 °, with step size and time of 0.01 ° and 0.2 s, respectively. Synchrotron high-resolution X-ray diffraction (HR-XRD) characterization was carried out at beamline P02.1, PETRA III electron storage ring (Deutsches Elektronen-Synchrotron, DESY, Hamburg) with a wavelength of 0.20735 Å in a spinner setup. A LaB_6 (NIST 660c) standard was measured to account for instrumental contributions. Rietveld refinement analysis of diffraction data was performed using FullProf Suite software[49]. The resolution parameters of the diffractometer were determined from the Rietveld refinement of XRD data for a LaB_6 standard. For sintered materials, the microstructure of the surfaces and fracture faces was examined by Scanning Electron Microscopy (SEM, LEO Gemini 1530, Carl, Zeiss, Germany) with an in-lens detector. Energy-dispersive X-ray spectroscopy (EDS, Thermo Fisher Scientific Inc., USA) mapping was further used to examine elemental distribution. The chemical/ oxidation states of cations were determined by X-ray photoelectron spectroscopy (XPS) on ESCALAB 250Xi (Thermo Fisher Scientific, USA). The size of the X-ray spot on the sample was 100 μm. All X-ray photoelectronic spectra were calibrated using the C1s core line with a binding energy of 284.8 eV. X-ray absorption fine structure (XAFS) measurements for the Mn K edge were carried out with a self-developed wavelength-dispersive spectrometer in von Hámos geometry[50,51]. The spectrometer is equipped with a microfocus X-ray tube with molybdenum as anode material, a curved highly annealed pyrolytic graphite mosaic crystal, and a hybrid photon counting CMOS detector with 512×1030 pixel and a pixel size of 75×75 μm. The tube was operated with a high voltage of 12 kV and a current of 1520 μA for the measurement. The reference samples MnO_2 and Mn_2O_3 were prepared as powders on adhesive tape, the reference sample hexagonal $SrMnO_3$ and the sample HEPO were prepared with Hoechst Wax as a pellet, due to its lower concentration of Mn, with 13 mm pellet diameter. The samples and references were measured in transmission and were constantly moved during the measurements to minimize the effects of local thickness inhomogeneity. The beam size on the samples is around 3×3 mm. For the normalization of the data and further analysis of the spectra, ATHENA of the Demeter software package has been used[52]. The measurement time for the reference samples was 2.5 h while the sample HEPO was measured for 62.5 h, due to its low manganese content and the high absorption by the strontium. The measurement of the compressive strength of printed samples was conducted in a universal testing machine RetroLine (Zwick/Roell, Germany) equipped with a 20 kN load cell between flat platens at a crosshead speed of 0.5 mm/min. To prepare test samples, the woodpile-structured specimens were cut into plates with a wire saw to achieve relatively parallel surfaces and a thickness of a plate of about 8 mm, while the diamond lattice-structured samples were left intact because of their fragile structure.

3. Results and discussion

3.1. Development of photocurable resins for printing and mechanism of DLP fabrication

The photocurable resins with multimetallic polymeric precursors for DLP fabrication of ceramics should fulfill several requirements, such as (i) polymerizability under illumination at a given wavelength with sufficient cross-linking to achieve moderate strength and low volume shrinkage to avoid distortions in the fabricated objects, (ii) the rheological properties (viscosity) of the resins suitable for printing process, and (iii) the components of resins and their decomposition products should be completely removable during thermal treatment (debinding and sintering). Considering the above restrictions, we have successfully developed printable precursor-containing resins with AA as the monomer, GDD as the cross-linker, Sudan orange G as a photoinitiator, and TPO-L as a photon absorber. GDD was used due to its solubility in ethylene glycol, the photoinitiator and the photon absorber on the basis

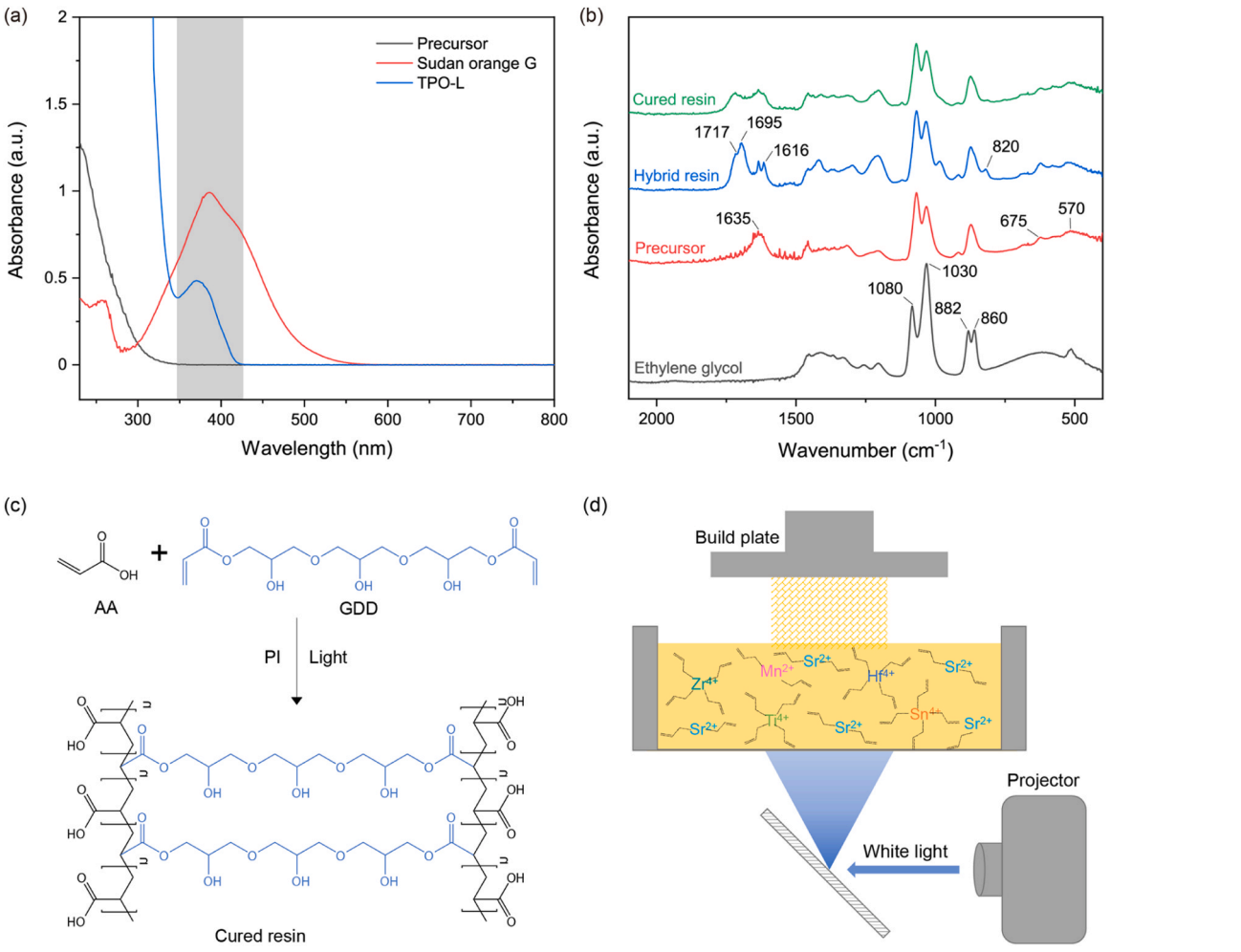

Fig. 1. (a) UV-Vis absorption spectra of diluted multimetallic polymeric precursor, Sudan orange G and TPO-L. The gray area is the effectively utilized waveband, covering the overlapping absorption range of the photoinitiator and photon absorber. (b) FTIR spectra of ethylene glycol and resin at different stages of polymerization and processing. (c) Schematic of photopolymerization mechanism of AA and GDD. (d) Schematic of the DLP fabrication with the resin developed in this work. The yellow liquid in the bath represents the hybrid resin and the yellow pattern represents the printed thermoset with homogenously and randomly distributed metal cations in the polymeric network.

of their optical properties (Fig. 1a). The precursor is transparent in the working wavelength range, TPO-L displays strong absorption below 340 nm as well as a weak absorption peak between 340 and 420 nm, which coincides with the wavelength range of our light source and the absorption wavelength range of Sudan orange G. Due to the weak absorption of the photoinitiator in the visible range, the concentration of the photon absorber in the resin was set at 0.01 wt%, and the exposure time of each print layer was set at 40 s.

The molecular structure of the resin as well as the curing process were monitored by FTIR, for comparison reasons the spectra of ethylene glycol and precursor were also recorded (Fig. 1b). The adsorption bands at 1080 and 1030 cm^{-1} can be attributed to the C-O stretching vibrations and the bands from 882 to 860 cm^{-1} are assigned to the C-H deformation vibrations of ethylene glycol. The absorbance band at 1635 cm^{-1} in the precursor is the H-O-H scissor bending vibration of water[53]. The FTIR spectrum of the polymeric precursor confirms the complexation of cations by ethylene glycol, which can be seen from the intensity change of the band characteristic to ethylene glycol as well as the appearance of new bands at around 675 and 570 cm^{-1} attributed to the metal-oxygen stretching vibrations (which were not observed in ethylene glycol) [54,55]. With the addition of acrylic acid, new bands at 1616 cm^{-1} and 820 cm^{-1} characteristic for C═C stretching and bending vibrations in AA [56] appear; these bands disappear completely after curing. Another important aspect is the complexation of metal cations by acrylic acid, which is seen from the shift of the adsorption band characteristic of -C═O stretching vibration of carboxylate groups from 1717 cm^{-1} in pure AA (-COOH) to 1695 cm^{-1} in the hybrid resin ($-COO^-$) [57].

These data suggest the following mechanism of the photopolymerization during the DLP printing process (Fig. 1c). When exposed to light with wavelengths in the range of 380–420 nm, the TPO-L decomposes to free radicals, which activate the unsaturated -C═C- bonds of AA and GDD and lead to cross-linking and polymerization, as indicated by the disappearance of the -C═C- bands in FTIR spectra (Fig. 1b). The AA undergoes chain growth polymerization, while GDD links the long chains to form a cross-linked network. As a result, the complexed cations are becoming homogenously and randomly distributed in the cross-linked polymeric network of the printed thermosets (Fig. 1d).

3.2. Selection of heat treatment and sintering

All resins developed in this work have been successfully used for the DLP fabrication of complex rubber-like parts (printed thermosets) that exhibit high print accuracy and moderate strength and elasticity (Fig. S2 a-d). Transformation of the thermosets into ceramics requires thermal treatment steps i.e., debinding and sintering, which could lead to severe shrinkage and cracking due to the decomposition of the resin components. Therefore, the suitable thermal treatment process was selected on

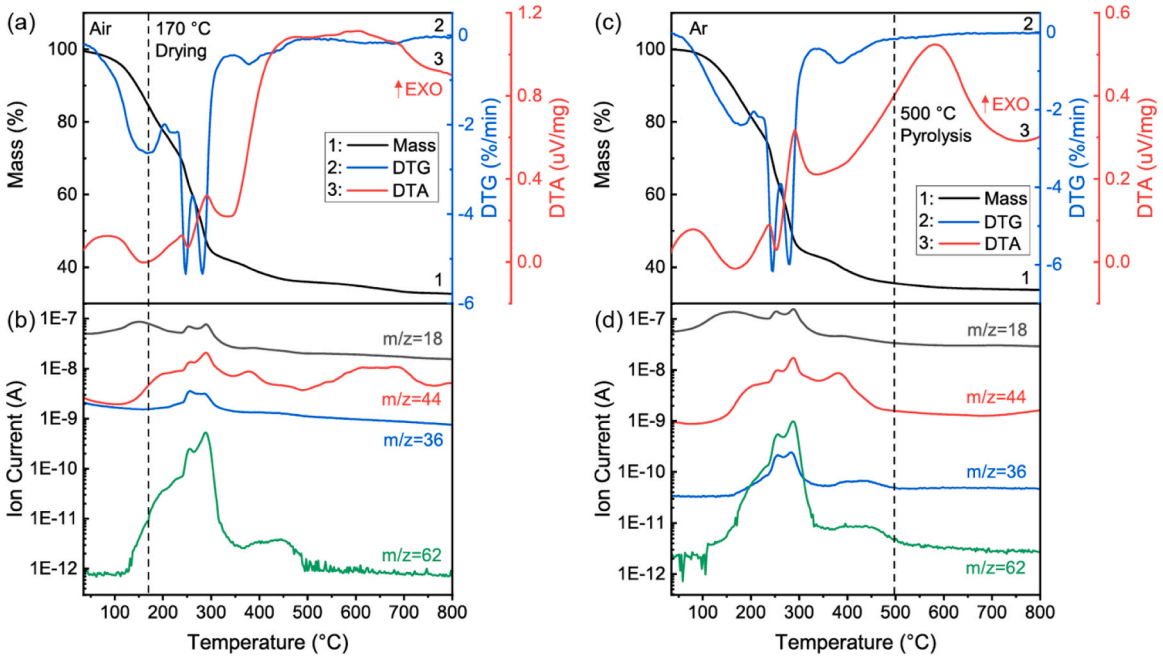

Fig. 2. Results of (a) simultaneous thermal analysis coupled with (b) mass spectrometry of the printed PEG-0 thermoset in air. Results of (c) simultaneous thermal analysis coupled with (d) mass spectrometry of the printed PEG-0 thermoset in argon.

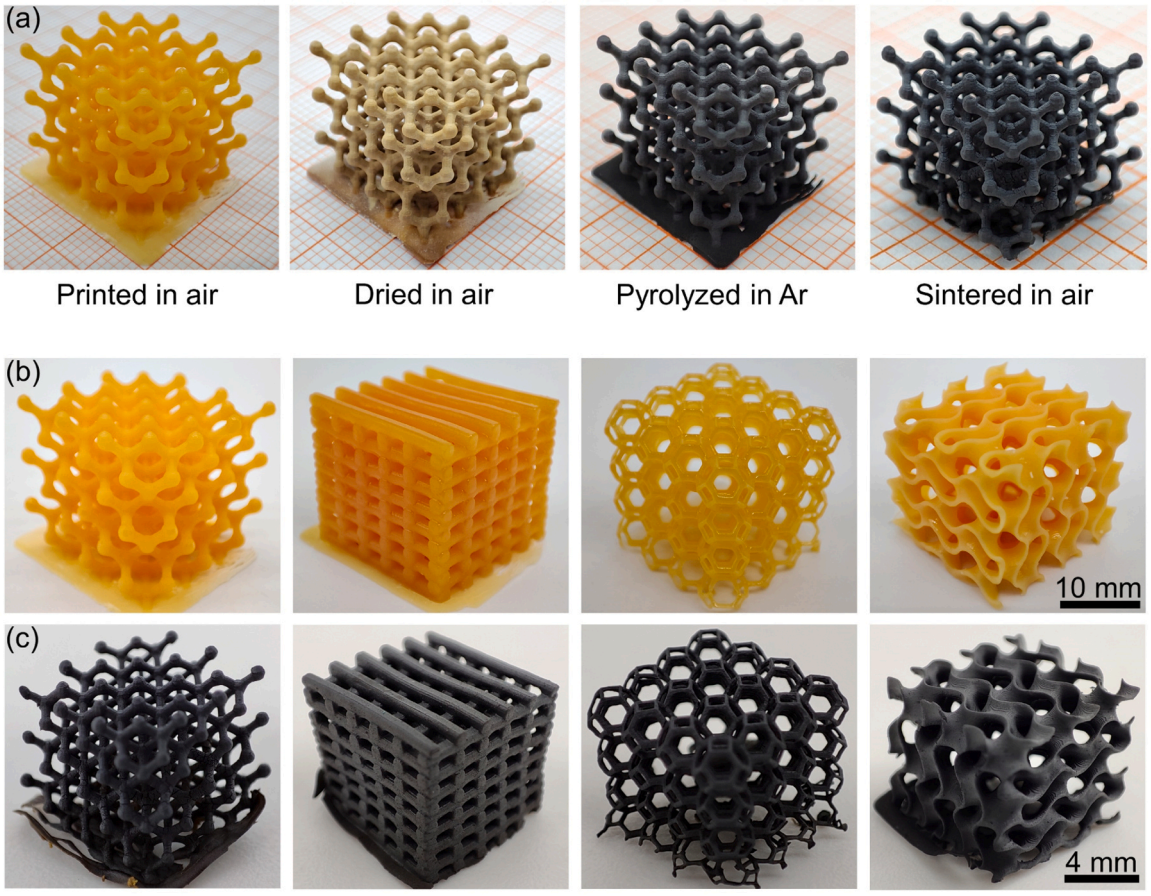

Fig. 3. (a) Optical images of a representative specimen fabricated with PEG-3 resin at different stages of heat treatment. The sample was placed on squared paper, where each small grid is 1 mm^2. (b, c) Optical images of four different sample geometries /shapes: (b) PEG-2-thermosets after DLP fabrication, (c) those sintered at 1500 °C. From left to right: (i) diamond lattice structure, (ii) woodpile structure, (iii) cubic lattice with truncated octahedron (tetradecahedron) unit cells, (iv) Gyroid-type triply periodic minimal surface structure.

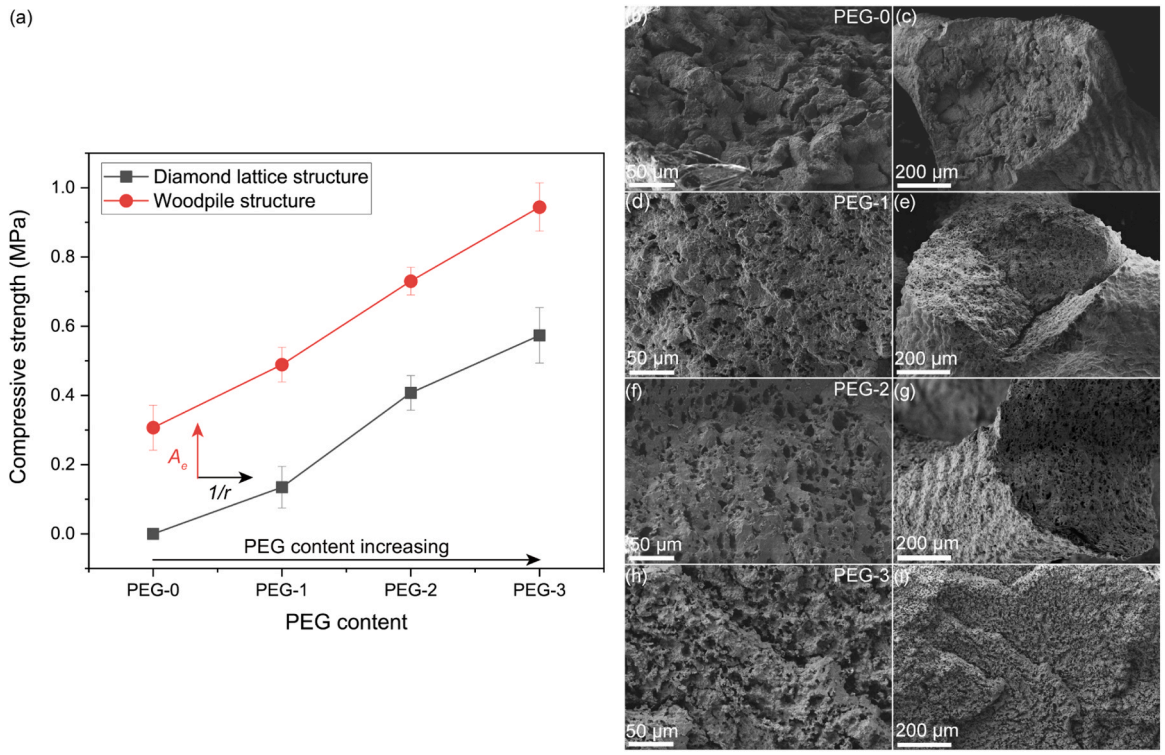

Fig. 4. (a) Compressive strength of the specimens printed with diamond lattice and woodpile structure and sintered at 1500 °C; according to Griffith fracture theory (see eq. 3 below), the compressive strength increases with decreasing average radius of the pores (r), which in turn decreases with PEG content, and increasing the fraction of the effective area (A_e), which in turn is large for woodpile structure. All error bars represent standard deviations, and test number n = 5. (b) SEM images of the fractured surfaces of PEG-0–1500 (b, c), PEG-1–1500 (d, e), PEG-2–1500 (f, g), and PEG-3–1500 (h, i) specimens.

the basis of the STA analysis of specimens carried out in argon and air (Fig. 2a-d) and realized in three steps as described below. When heated in argon, the first significant mass loss (~20 %) from 100 to 200 °C with an endothermic peak corresponds to the evaporation of residual ethylene glycol (m/z=62) and H_2O (m/z=18) from the printed sample. From 240–300 °C a further endothermic process with around 30 % mass loss occurred, which is attributed to the decomposition of the resin components releasing gaseous species such as ethylene glycol, CO_2 (m/z=44), H_2O (m/z=18), and HCl (m/z=18). The weight stabilization is observed at temperatures above 700 °C with a ceramic yield of about 30 wt% and a linear shrinkage of around 50 %. The thermal decomposition process of the specimens in air up to 500 °C is similar to that in argon. Above at 500 °C, an exothermic weight loss accompanied by CO_2 (m/z=44) release is observed, which is likely to be the oxidation (burn-off) of carbon residuals formed during the decomposition of resin components. The samples thermally decomposed at 500 °C in air have more cracks than those pyrolyzed in argon. On the basis of these data, the following thermal treatment process was realized: (i) the printed thermosets were first dried in air at 170 °C for 24 h to slowly evaporate the excess ethylene glycol; (ii) to reduce cracks, the dried samples were subsequently pyrolyzed at 500 °C under argon flow with a low heating rate of 0.3 °C/min; and (iii) finally, the specimens were sintered in air at 1500 °C for 1 h.

The above-developed thermal debinding and sintering procedure was applied to the fabricated thermosets (see Fig. S2 e-h). The sintered ceramic part fabricated from the PEG-0 resin without the addition of PEG remains very fragile and porous and exhibits a number of cracks, in addition, some branches of the diamond crystal structure were lost after sintering (see Fig. S2e). This is the result of a strong gas release and enormous internal stress during heat treatment. Therefore, a suitable polymeric binder was applied for reducing pore size which in turn should reduce the number of cracks. Typical examples of them are polyvinyl alcohol, ethylene glycol citrate polyester, and PEG. Despite their excellent solubility in ethylene glycol, polyvinyl alcohol and ethylene glycol citrate polyester are not suitable because they significantly increase the viscosity of the resin and thus impair the kinetics of photopolymerization. PEG has a higher decomposition temperature (~400 °C) than our hybrid resin [58], which makes it a useful binder in the early phase of pyrolysis. The maximum amount of PEG that can be added to the resin is limited due to its interaction with metal cations in the resin, the complexation of metal cations with PEG results in a cloudy suspension [59]. PEG in the range of 1–3 wt% had no significant influence on the resin viscosity and in turn on the printing accuracy. All those factors make PEG a suitable binder for the DLP fabrication with miltimetallic polymeric precursors. The surface of the PEG-1–1500 specimen is smoother than that of PEG-0–1500 (Fig. S2f), but some branches of the diamond crystal structure are still missing. In contrast, the PEG-2–1500 and PEG-3–1500 specimens maintain the printed shape without cracks after sintering (Fig. S2g, h); this is due to “pore generation” during the decomposition of the porogen PEG. The decomposition of PEG at ~400 °C results in uniformly distributed micro-sized pores preventing in this way from cracking (Fig. 4). After pyrolysis and sintering the PEG-containing samples retained their original shape with no noticeable cracks, as exemplarily shown for the PEG-3–1500 specimen at different stages of heat treatment (Fig. 3a). Fig. 3b and c display the optical images of four different geometries /shapes after DLP fabrication and sintering at 1500 °C, representatively taken for the PEG-2 resin: (i) a diamond-like lattice in which none of the branches of this structure is parallel or perpendicular to the horizontal plane, (ii) a woodpile structure consisting of a finite stack of lattices, each of which consists of a planar collection of identical rods (“struts”); each lattice is parallel to the xz-plane, and the cylinders in each layer are orthogonal to the cylinders in the neighboring layers, (iii) a cubic lattice of truncated octahedrons (or tetradecahedrons) (iv) a Gyroid-type triply periodic minimal surface structure. These results show that DLP manufacturing with our printable resins has high dimensional fidelity and can be used to produce a variety

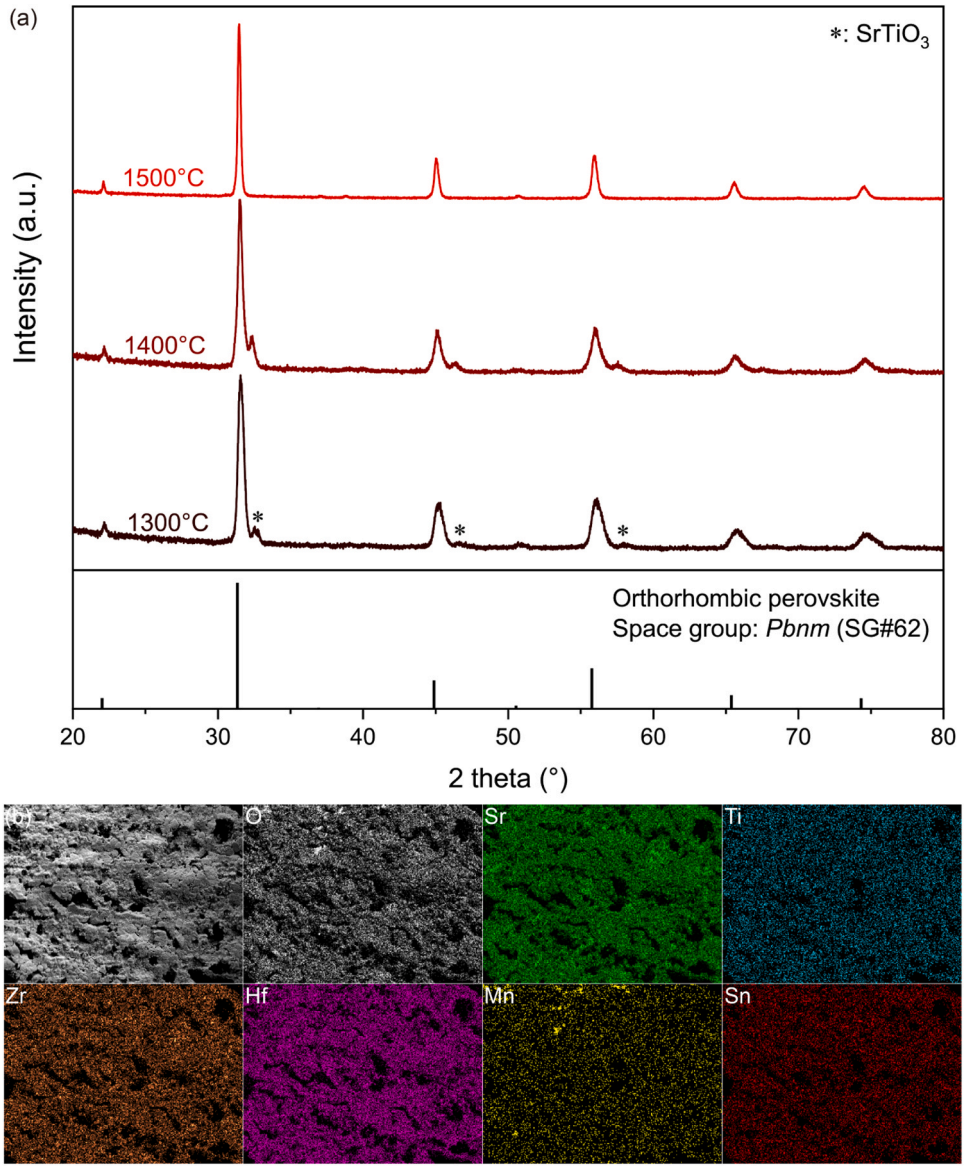

Fig. 5. (a) The XRD patterns (λ = 1.5406 Å) of the specimen PEG-3 after sintering at different temperatures. (b) EDS elemental mapping of the surface of specimen PEG-3 sintered at 1500 °C. The benchmark Bragg position was calculated by the Rietveld refinement based on the high-resolution synchrotron XRD data (λ = 0.2073 Å) of PD5–1000 (see Fig. 8).

of shapes that are retained in the ceramic parts after carefully controlled thermal debinding and sintering.

3.3. Mechanical properties and microstructure

Compressive tests were carried out on the samples printed with diamond- and woodpile-type structures and sintered at 1500 °C (Fig. 4). The samples with a diamond-lattice structure showed rather low compressive strength; for example, we could not measure the compressive strength of PEG-0–1500 specimen with a diamond-lattice structure using our mechanical testing equipment. The compressive strength of the samples with a woodpile structure is significantly higher than that of the samples with a diamond lattice structure at the same PEG content. The mechanical strength of both printed structure types increases with increasing the PEG content, and the PEG-3–1500 specimens exhibit the highest compressive strength of 0.57 MPa and 0.94 MPa for diamond lattice and woodpile structures, respectively. Since none of the branches of the diamond-type geometry are parallel or perpendicular to the horizontal plane, they are subjected to a significant bending moment during the compression test, resulting in low mechanical strength and rapid failure. A "simple" woodpile structure consisting of a series of parallel struts with alternating alignments exhibits significantly higher mechanical stability in the compression test.

Fig. 4 displays the SEM images of the fracture surface of the samples studied. As shown in Fig. 4b, c, several irregularly shaped macropores (~40 μm) are observed on the fracture surface of the PEG-0–1500 specimen. During pyrolysis, these pores are the result of the evolution of gaseous products, which accumulate and cannot be discharged smoothly, with the associated stresses leading to deformation and cracking. Therefore, the fracture surfaces of PEG-0–1500 and PEG-1–1500 demonstrate large-size cracks of about ~200 μm (Fig. 4b-e). The smooth fracture surface of PEG-2–1500 (Fig. 4f, g) confirmed that a brittle fracture had occurred. The fracture surface of the PEG-2–1500 and PEG-3–1500 samples exhibit small round pores of ~5 μm in diameter that are evenly distributed and the material between the pores is dense, resulting in fewer defects and better compressive strength. Neighboring pores in PEG-3–1500 (Fig. 4h, i) are in contact with each other and form interconnected channels, which favors the release of

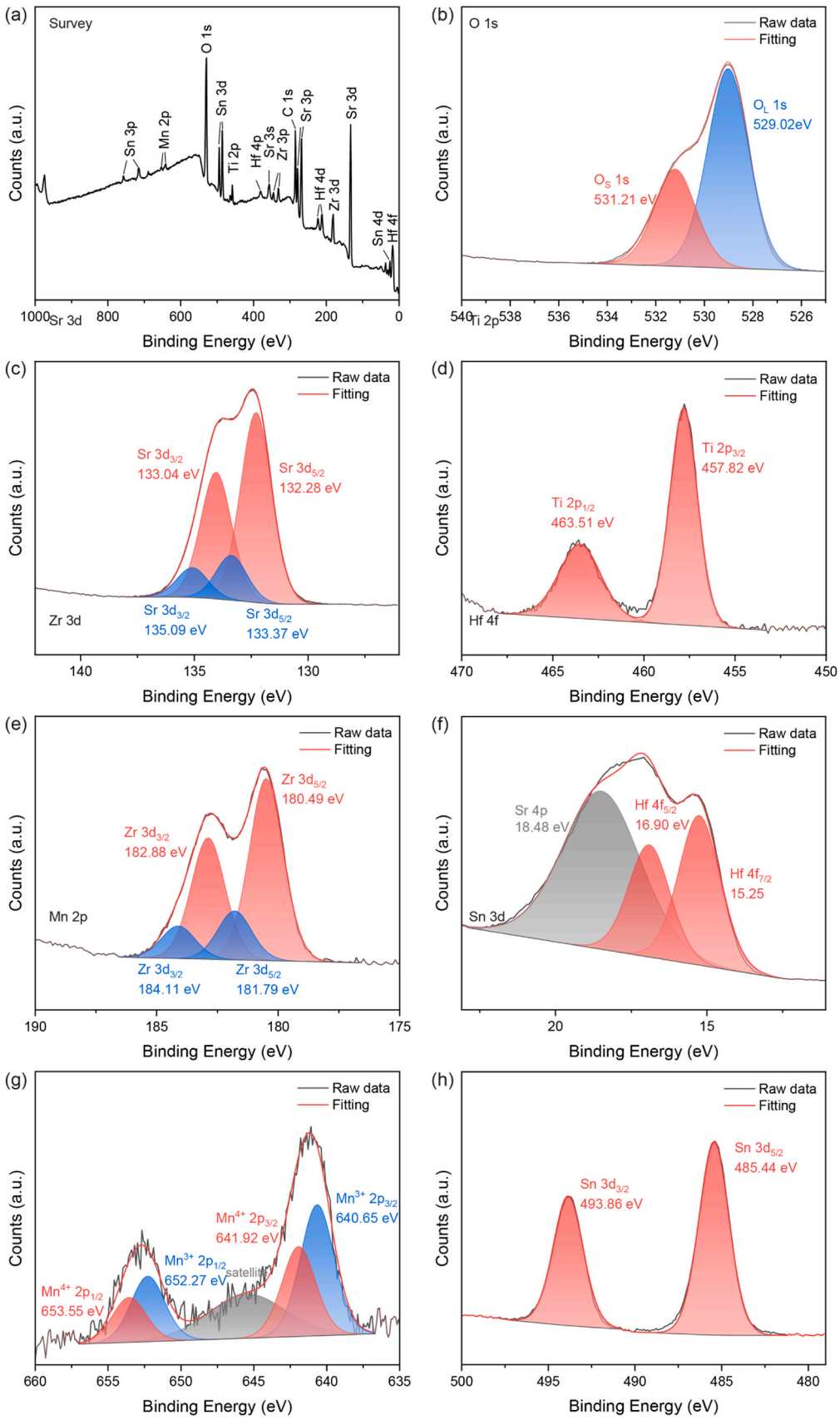

Fig. 6. X-ray photoelectron spectra of the PEG-3–1500 specimen: (a) the survey spectrum; (b-h) the high-resolution O1s, Sr3d, Ti3d, Zr3d, Hf4f, Mn2p, and Sn3d regions. The red curves represent the measured data, and the black curves represent the fitting results.

Table 2
The chemical states of elements in the PEG-3–1500 sample studied by XPS.

Element	Peaks	Binding energy (E_B), eV	Interpretation	Reference
Sr	$3d_{3/2}$ / $3d_{5/2}$	132.28 / 134.04	Sr^{2+} in $SrSnO_3$	[68]
		135.09 /133.37	Hydroxylated Sr^{2+} at the surface	[69]
Sn	$3d_{3/2}$ / $3d_{5/2}$	485.44 / 493.86	Sn^{4+} in $SrSnO_3$	[68]
Ti	$3p_{1/2}$ / $3p_{3/2}$	463.51/ 457.82	Ti^{4+} in $SrTiO_3$	[70]
Zr	$3d_{3/2}$ / $3d_{5/2}$	182.88 / 180.49	Zr^{4+} in $SrZrO_3$	[71]
		184.11/ 181.79	Hydroxylated Zr^{4+} at the surface	[69]
Hf	$4f_{5/2}$ / $4f_{7/2}$	16.90 / 15.25	Hf^{4+} in $SrHfO_3$; E_B is smaller by about 1.6 eV compared with those of $SrHfO_3$	[72]
Mn	$2p_{3/2}$ / $2p_{5/2}$	641.92 / 653.55	Mn^{4+} in $SrMnO_{3-x}$ perovskite	[64,65]
		652.27/ 640.65	Mn^{3+} in $SrMnO_{3-x}$ perovskite	[64,65]
O	1 s	530.94	surface oxygen in hydroxyl/ carbonate groups	[73]
		528.91	lattice oxygen	

gaseous products and preserves the overall sample geometry /form. These pores allow gases to discharge smoothly and reduce stress concentration during the heat treatment process. According to the Griffith fracture theory, the compressive strength of brittle materials is influenced by the size of the pores. For a given porosity, smaller pores lead to a higher compressive strength[60,61] [62]. :

$$\sigma_p = \sqrt{\frac{2EA_e\lambda}{\pi Kr}}\# \quad (1)$$

where E is the elastic modulus of solid bulk material, and A_e is the fraction of the effective area; λ is the surface energy; K is the constant related to the shape of pores, and r is the average radius of the pores. The addition of PEG eliminates the larger macropores and higher PEG content results in a more uniform pore size distribution with fewer oversized pores, effectively reducing the stress concentration. This is a reason for an increase in compressive strength with increasing PEG content. For a given pore size the compressive strength is high for geometries/lattices with an increasing fraction of the effective area, which is indeed observed for the woodpile-type lattice compared with those with diamond-type geometry (see Fig. 4a). Summarizing, the fabrication of complex structures of high-entropy perovskite-type oxide ceramics with considerable strength can be achieved through geometric design and the addition of porogens (i.e. PEG).

3.4. Structure and elemental distribution

Since the PEG content does not influence the phase composition in the materials under study (i.e. same phase composition was observed for all specimens after sintering, see Fig. S3), a sample with the highest compressive strength i.e., PEG-3–1500, was selected for the detailed compositional and structural analysis. The change in phase composition as a function of sintering temperature was monitored by XRD (Fig. 5a). The strong XRD reflection at 2θ of 31.5 ° is attributed to a perovskite solid solution, while the weak reflection at about 32.5 ° observed after sintering at 1300 and 1400 °C corresponds to the (110) plane of perovskite-type $SrTiO_3$ [63]. With increasing temperature, the neighboring reflections of these two phases gradually merged, until a single-phase composition is formed, resembling the formation process of high-entropy carbides observed in our previous work [47]. The XRD pattern of the PEG-3–1500 sample is similar to the pattern of perovskite-type $Sr(Ti_{0.2}Zr_{0.2}Hf_{0.2}Mn_{0.2}Sn_{0.2})O_3$ material reported recently [3]. The EDS mapping confirmed the uniform distribution of most cations (Fig. 5b), confirming the formation of the homogeneous high-entropy perovskite-type material. The observation of Mn-enriched regions (Fig. 5b) suggests that the minor manganese segregation on the surface is in trace amounts with the amorphous component. A side Mn-containing phase was not detected by either XRD or HR-XRD.

3.5. Elemental composition and oxidation state of the cations

The elemental composition of the PEG-3–1500 specimen was determined by ICP-OES (Table S1), EDS (Fig. S4), XPS, and oxygen analyzer. The comparison of this data is discussed later in this work. First, we address the oxidation state of cations in this specimen studied by XPS (Fig. 6 and Table 2) and XAFS (Fig. 7). Remarkably, all peaks in the X-ray photoelectronic spectra can be assigned to the chemical states of the elements in the corresponding perovskites, which in turn confirms the formation of the perovskite-type structure in the sample. The Mn $2p_{3/2}$/ $2p_{1/2}$ doublet at 641.92 / 653.55 eV can be assigned to Mn^{4+}, those at 640.65 / 652.27 eV are attributed to Mn^{3+}, which is consistent with previous reports for $SrMnO_{3-x}$ perovskite[64,65]. A high content of adsorbed oxygen (~40 at%) can be attributed to the defects on the surface, i.e., oxygen vacancies[66,67]; the oxygen non-stoichiometry is confirmed by elemental analysis as well, which gives 19.5 wt% oxygen, slightly less than the theoretical value of 20.5 wt% for a stochiometric

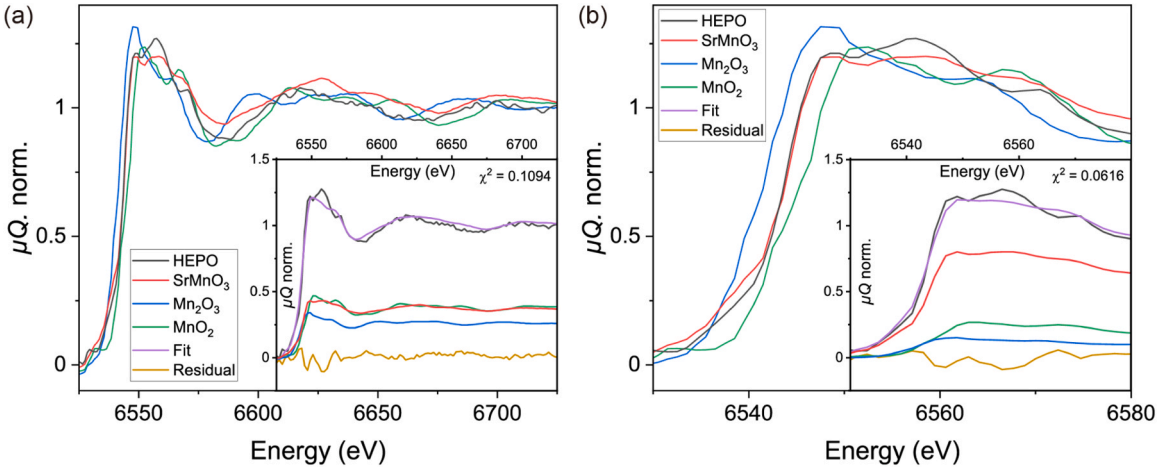

Fig. 7. The normalized (a) XAFS and (b) XANES spectra at the Mn K-edge of the PEG-3–1500 specimen along with the reference materials $SrMnO_3$, MnO_2, and Mn_2O_3. Inserted are the LCF fitting curves of spectra with all three reference materials.

Table 3
Composition of the PEG-3–1500 sample from XPS, EDS, ICP-OES, and XAFS/XANES analysis.

Cation	Cationic fraction, at%				
	Targeted	XPS	EDS	ICP-OES	XAFS & XANES[a])
Sr^{2+}	50	57.10	46.27	50.05	-
Ti^{4+}	10	6.54	11.93	10.95	-
Zr^{4+}	10	11.24	11.02	10.92	-
Hf^{4+}	10	17.94	13.76	11.58	-
Mn^{3+}	10	0.97	7.47	7.45	1.40
Mn^{4+}		0.67			6.05
Sn^{4+}	10	5.54	9.55	9.05	-

[a]The Mn^{3+} and Mn^{4+} fractions are calculated from the total Mn amount from ICP-OES.

perovskite structure.

To calculate the fraction of the Mn^{3+} and Mn^{4+} cations, XAFS measurements were performed at Mn K-edge with $SrMn^{4+}O_3$, $Mn^{4+}O_2$, and $Mn_2^{3+}O_3$ as reference materials. The normalized spectra are presented in Fig. 7a. Even after a measurement period of 62.5 hours, the sample spectra have a low signal-to-noise ratio compared to the reference spectra, which complicates a quantitative interpretation. From the qualitative comparison of the sample with the references, the highest agreement (especially when comparing the edge position) is found with the $SrMnO_3$ reference with Mn^{4+} cations. A linear combination fit (LCF) of the sample spectrum with the reference spectra $SrMn^{4+}O_3$, $Mn^{4+}O_2$, and $Mn_2^{3+}O_3$ (with all possible combinations of three references) was performed to estimate the fraction of Mn^{3+} and Mn^{4+}. An LCF was applied to both the region of the X-ray absorption structure near the edge (XANES) (6525–6595 eV) and the whole spectrum (6525–6725 eV) separately. The results for the LCF are inserted in Fig. 7b for the XANES range and in Fig. 7a for the entire spectrum. In each case, the summed 4+ oxidation state is above 70 wt% (Table S2 and S3), but it should be noted that the best agreement is obtained when all three references are considered. From the results, especially considering the lower SNR of the PEG-3–1500 sample compared to the references and the sometimes strongly oscillating residual in the LCFs, missing species cannot be excluded. For the following discussion and presentation of the specimen composition, we take the mean value of the LCF results of the XAFS and XANES with all three reference materials, i.e. the atomic ratio of Mn^{4+} to Mn^{3+} as 81.25–18.75.

The cation content calculated from the ICP-OES and EDS data deviates slightly from the targeted stoichiometry (Table 3). Since XPS is a surface-sensitive method, the XPS results only reflect the approximate element content of the surface; these data are not considered by calculating the elemental composition. Considering the accuracy of quantitative EDS analysis, we use the ICP-OES data and take into account the oxygen content determined by the elemental analyzer. To summarize, the PEG-3–1500 specimen in the high-entropy perovskite-type oxide with the composition $Sr(Ti_{0.22}Zr_{0.22}Hf_{0.23}Mn_{0.15}Sn_{0.18})O_{2.85}$, in which manganese is considered to be in two oxidation states, that is, Mn^{3+} and Mn^{4+} with the atomic ratio of Mn^{4+} to Mn^{3+} of about 81.25–18.75.

3.6. Structural model

The crystal structure of synthesized high-entropy perovskite-type oxide $Sr(Ti_{0.22}Zr_{0.22}Hf_{0.23}Mn_{0.15}Sn_{0.18})O_{2.85}$ was determined from the Rietveld refinement of synchrotron HR-XRD pattern using DICVOL06 and CheckGroup programs implanted in Fullprof software as described in the supporting information. The results of indexing of the XRD pattern, LeBail fitting, and space group checking suggested that the Sr $(Ti_{0.22}Zr_{0.22}Hf_{0.23}Mn_{0.15}Sn_{0.18})O_{2.85}$ material is crystallized in orthorhombic rather than cubic or monoclinic structures. Our results are in good agreement with previous works in the literature that reported the same space group for $Sr^{2+}B^{4+}O_3$ perovskites (B = Hf, Ti, Zr, Sn, etc, see Supporting Information Page 9)[74–79]. The final cycle of Rietveld refinement analysis for the XRD pattern of the Sr $(Ti_{0.22}Zr_{0.22}Hf_{0.23}Mn_{0.15}Sn_{0.18})O_{2.85}$ (i.e. PEG-3–1500 specimen) using the suggested orthorhombic (*Pbnm*) structure is shown in Fig. 8a. Structure parameters, Rietveld R-factors, and atom positions of the orthorhombic structure are given in Table 4. The B-site in HEPO is assumed to be occupied uniformly by five different cations with different radii, some of which exhibit large radii (e.g., Zr^{4+} and Hf^{4+}), resulting in oxygen octahedral tilting as shown in Fig. 8b.

4. Conclusions

A high-entropy perovskite-type oxide with a composition Sr $(Ti_{0.22}Zr_{0.22}Hf_{0.23}Mn_{0.15}Sn_{0.18})O_{2.85}$ has been synthesized from a multimetallic polymeric precursor. The photocurable resins with multimetallic polymeric precursors were developed and applied for the DLP fabrication of complex rubber-like parts with high printing accuracy and moderate strength and elasticity. Through thermal debinding and sintering at ambient pressure, the thermosets were transformed to high-entropy perovskite-type oxides with retention of the printed geometry. Applied as a binder and porogen, polyethylene glycol greatly reduced cracks and created uniformly distributed micron-sized pores, lending to improved compressive strength, which reaches 0.94 MPa for the woodpile-type structure specimen fabricated with 3 wt% PEG and

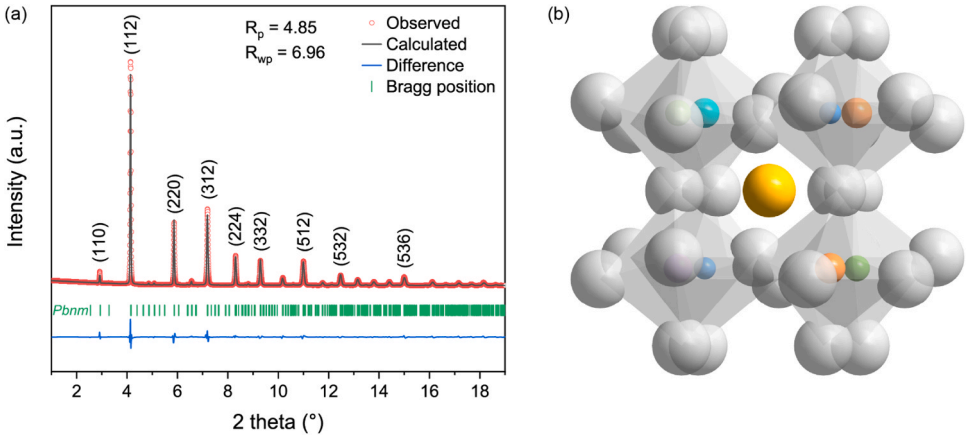

Fig. 8. (a) Rietveld refinement of synchrotron HR-XRD data (λ = 0.2073 Å) collected on the PEG-3–1500 specimen. (b) Cubic perovskite lattice with orthorhombic distortion. The gray spheres represent O^{2-} and form the tilted oxygen octahedron. The large yellow spheres represent Sr^{2+}, and the smaller colored spheres represent homogeneously and randomly distributed B-site Ti^{4+}, Zr^{4+}, Hf^{4+}, Mn^{3+}, Mn^{4+}, and Sn^{4+} cations.

Table 4
Structure parameters from crystal structure refinement for $Sr(Ti_{0.22}Zr_{0.22}Hf_{0.23}Mn_{0.15}Sn_{0.18})O_{2.85}$ in Space Group *Pbnm* (No. 62)[a].

Atoms	Wyckoff position	x[b]	y[b]	z[b]	Biso(Å^2)[c]	Occupation factor
Sr (1)	4c	−0.0026(9)	0.5089(4)	1/4	1.112(16)	0.50052
Ti (1)	4a	0	0	0	0.169(11)	0.10951
Zr (1)						0.10919
Hf (1)						0.11575
Mn (1)						0.07450
Sn (1)						0.09053
O (1)	4c	−0.0140(27)	−0.0010(27)	1/4	0.553(15)	0.47560
O (2)	8d	0.2452(40)	0.2781(22)	0.0419(9)	0.553(15)	0.95120

[a] $a = 5.7007(3)$ Å, $b = 5.7326(2)$ Å, $c = 8.1043(2)$ Å, and $D = 5.846$ g/cm^3; $R_p = 4.85$ %, $R_{wp} = 6.96$ %, $R_f = 4.46$ %, and $R_B = 3.31$ %.
[b] Fractional atomic coordinates.
[c] Isotropic temperature factors.

sintered at 1500 °C. The orthorhombic crystal structure is identified by the Rietveld refinement of high-resolution synchrotron X-ray structure analysis; the elemental and spectroscopic characterizations suggest the composition $Sr(Ti_{0.22}Zr_{0.22}Hf_{0.23}Mn_{0.15}Sn_{0.18})O_{2.85}$. The DLP fabrication of high-entropy perovskite-type oxides such as the studied material, and the composition-driven occurrence of octahedral tilting in this structure, with its associated influence on the functional properties of this material, open up new directions for the novel materials in emerging applications requiring the additive manufacturing of functional materials in intricate geometries, including advanced electronic components and integrated capacitors. This work represents the first time that the additive manufacturing of high-entropy ceramics has been realized, further broadening the toolset of ceramic additive manufacturing in general and perovskite engineering in particular.

CRediT authorship contribution statement

Haotian Yang: Conceptualization, Methodology, Investigation, Data curation, Formal analysis, Writing – original draft. **Xifan Wang:** Methodology, Investigation. **Sebastian Praetz:** Investigation, Data curation, Formal analysis. **Shumin Pang:** Investigation. **Oliver Görke:** Investigation. **Maged F. Bekheet:** Investigation, Data curation, Formal analysis, Writing – review & editing. **Dorian A.H. Hanaor:** Writing – review & editing, Supervision. **Aleksander Gurlo:** Conceptualization, Resources, Writing – review & editing, Supervision.

Declaration of Competing Interest

The authors declare that they have no known competing financial interests or personal relationships that could have appeared to influence the work reported in this paper.

Acknowledgments

This work was supported by the China Scholarship Council (201907565035). We would like to acknowledge Delf Kober for the STA-MS measurement, Huaiyou Chen for the FTIR analysis, Maria Unterweger for the XPS test, and Ge Chen for the oxygen element analysis, all from Technische Universität Berlin. We also acknowledge Martin Etter, Henrik S. Jeppesen, and DESY (Hamburg, Germany), a member of the Helmholtz Association HGF, for the provision of experimental facilities. Parts of this research were carried out at PETRA III, beamline P02.1, under proposal ID (LTP II-20210010).

Supporting information

Supporting information includes results of the viscosity measurement, optical images of the printed and sintered samples, ICP-OEM analysis, XRD patterns of 1500 °C-sintered samples, EDS analysis, unnormalized raw XAFS spectra, linear combination fitting results, investigation of crystal structure, calculation of the Goldschmidt tolerance factor and the octahedral factor.

Appendix A. Supporting information

Supplementary data associated with this article can be found in the online version at doi:10.1016/j.jeurceramsoc.2024.116812.

References

[1] C.M. Rost, E. Sachet, T. Borman, A. Moballegh, E.C. Dickey, D. Hou, J.L. Jones, S. Curtarolo, J.-P. Maria, Entropy-stabilized oxides, Nat. Commun. 6 (2015), https://doi.org/10.1038/ncomms9485.
[2] R. Djenadic, A. Sarkar, O. Clemens, C. Loho, M. Botros, V.S.K. Chakravadhanula, C. Kübel, S.S. Bhattacharya, A.S. Gandhi, H. Hahn, Multicomponent equiatomic rare earth oxides, Mater. Res. Lett. 5 (2017) 102–109, https://doi.org/10.1080/21663831.2016.1220433.
[3] S. Jiang, T. Hu, J. Gild, N. Zhou, J. Nie, M. Qin, T. Harrington, K. Vecchio, J. Luo, A new class of high-entropy perovskite oxides, Scr. Mater. 142 (2018) 116–120, https://doi.org/10.1016/j.scriptamat.2017.08.040.
[4] J. Dąbrowa, M. Stygar, A. Mikuła, A. Knapik, K. Mroczka, W. Tejchman, M. Danielewski, M. Martin, Synthesis and microstructure of the (Co,Cr,Fe,Mn,Ni) 3 O 4 high entropy oxide characterized by spinel structure, Mater. Lett. 216 (2018) 32–36, https://doi.org/10.1016/j.matlet.2017.12.148.
[5] J. Gild, Y. Zhang, T. Harrington, S. Jiang, T. Hu, M.C. Quinn, W.M. Mellor, N. Zhou, K. Vecchio, J. Luo, High-entropy metal diborides: a new class of high-entropy materials and a new type of ultrahigh temperature ceramics, Sci. Rep. 6 (2016), https://doi.org/10.1038/srep37946.
[6] V. Braic, M. Balaceanu, M. Braic, A. Vladescu, S. Panseri, A. Russo, Characterization of multi-principal-element (TiZrNbHfTa)N and (TiZrNbHfTa)C coatings for biomedical applications, J. Mech. Behav. Biomed. Mater. 10 (2012) 197–205, https://doi.org/10.1016/j.jmbbm.2012.02.020.
[7] B. Ye, S. Ning, Da Liu, T. Wen, Y. Chu, One-step synthesis of coral-like high-entropy metal carbide powders, J. Am. Ceram. Soc. 102 (2019) 6372–6378, https://doi.org/10.1111/jace.16514.
[8] S. Wang, D. Jia, Z. Yang, X. Duan, Z. Tian, Y. Zhou, Effect of BN content on microstructures, mechanical and dielectric properties of porous BN/Si3N4 composite ceramics prepared by gel casting, 2013.
[9] X. Han, V. Girman, R. Sedlak, J. Dusza, E.G. Castle, Y. Wang, M. Reece, C. Zhang, Improved creep resistance of high entropy transition metal carbides, J. Eur. Ceram. Soc. 40 (2020) 2709–2715, https://doi.org/10.1016/j.jeurceramsoc.2019.12.036.
[10] R. Liu, H. Chen, K. Zhao, Y. Qin, B. Jiang, T. Zhang, G. Sha, X. Shi, C. Uher, W. Zhang, L. Chen, Entropy as a gene-like performance indicator promoting thermoelectric materials, Adv. Mater. 29 (2017) 1702712, https://doi.org/10.1002/adma.201702712.
[11] H. Chen, K. Jie, C.J. Jafta, Z. Yang, S. Yao, M. Liu, Z. Zhang, J. Liu, M. Chi, J. Fu, S. Dai, An ultrastable heterostructured oxide catalyst based on high-entropy materials: a new strategy toward catalyst stabilization via synergistic interfacial interaction, Appl. Catal. B: Environ. 276 (2020) 119155, https://doi.org/10.1016/j.apcatb.2020.119155.
[12] J.X. Yang, B.-H. Dai, C.-Y. Chiang, I.-C. Chiu, C.-W. Pao, S.-Y. Lu, I.-Y. Tsao, S.-T. Lin, C.-T. Chiu, J.-W. Yeh, P.-C. Chang, W.-H. Hung, Rapid fabrication of high-entropy ceramic nanomaterials for catalytic reactions, ACS Nano 15 (2021) 12324–12333, https://doi.org/10.1021/acsnano.1c04259.
[13] N. Nuraje, K. Su, Perovskite ferroelectric nanomaterials, Nanoscale 5 (2013) 8752–8780, https://doi.org/10.1039/C3NR02543H.
[14] V.C. Coletta, R.V. Gonçalves, M.I.B. Bernardi, D.A.H. Hanaor, M.H.N. Assadi, F.C. F. Marcos, F.G.E. Nogueira, E.M. Assaf, V.R. Mastelaro, Cu-modified SrTiO 3 perovskites toward enhanced water–gas shift catalysis: a combined experimental and computational study, ACS Appl. Energy Mater. 4 (2021) 452–461, https://doi.org/10.1021/acsaem.0c02371.
[15] H.J. Snaith, Present status and future prospects of perovskite photovoltaics, Nat. Mater. 17 (2018) 372–376, https://doi.org/10.1038/s41563-018-0071-z.

[16] G. Zhang, G. Liu, L. Wang, J.T.S. Irvine, Inorganic perovskite photocatalysts for solar energy utilization, Chem. Soc. Rev. 45 (2016) 5951–5984, https://doi.org/10.1039/C5CS00769K.
[17] L. Yang, X. Kong, F. Li, H. Hao, Z. Cheng, H. Liu, J.-F. Li, S. Zhang, Perovskite lead-free dielectrics for energy storage applications, Prog. Mater. Sci. 102 (2019) 72–108, https://doi.org/10.1016/j.pmatsci.2018.12.005.
[18] P. Tan, M. Liu, Z. Shao, M. Ni, Recent advances in perovskite oxides as electrode materials for nonaqueous lithium-oxygen batteries, Adv. Energy Mater. 7 (2017) 1602674, https://doi.org/10.1002/aenm.201602674.
[19] Y. Sharma, B.L. Musico, X. Gao, C. Hua, A.F. May, A. Herklotz, A. Rastogi, D. Mandrus, J. Yan, H.N. Lee, M.F. Chisholm, V. Keppens, T.Z. Ward, Single-crystal high entropy perovskite oxide epitaxial films, Phys. Rev. Mater. 2 (2018), https://doi.org/10.1103/PhysRevMaterials.2.060404.
[20] J. Ma, K. Chen, C. Li, X. Zhang, L. An, High-entropy stoichiometric perovskite oxides based on valence combinations, Ceram. Int. 47 (2021) 24348–24352, https://doi.org/10.1016/j.ceramint.2021.05.148.
[21] R. Banerjee, S. Chatterjee, M. Ranjan, T. Bhattacharya, S. Mukherjee, S.S. Jana, A. Dwivedi, T. Maiti, High-entropy perovskites: an emergent class of oxide thermoelectrics with ultralow thermal conductivity, ACS Sustain. Chem. Eng. 8 (2020) 17022–17032, https://doi.org/10.1021/acssuschemeng.0c03849.
[22] S. Zhou, Y. Pu, Q. Zhang, R. Shi, X. Guo, W. Wang, J. Ji, T. Wei, T. Ouyang, Microstructure and dielectric properties of high entropy Ba (Zr0.2Ti0.2Sn0.2Hf0.2Me0.2)O3 perovskite oxides, Ceram. Int. 46 (2020) 7430–7437, https://doi.org/10.1016/j.ceramint.2019.11.239.
[23] J. Yan, D. Wang, X. Zhang, J. Li, Q. Du, X. Liu, J. Zhang, X. Qi, A high-entropy perovskite titanate lithium-ion battery anode, J. Mater. Sci. 55 (2020) 6942–6951, https://doi.org/10.1007/s10853-020-04482-0.
[24] T.X. Nguyen, Y.-C. Liao, C.-C. Lin, Y.-H. Su, J.-M. Ting, Advanced high entropy perovskite oxide electrocatalyst for oxygen evolution reaction, Adv. Funct. Mater. 31 (2021) 2101632, https://doi.org/10.1002/adfm.202101632.
[25] P. Edalati, Q. Wang, H. Razavi-Khosroshahi, M. Fuji, T. Ishihara, K. Edalati, Photocatalytic hydrogen evolution on a high-entropy oxide, J. Mater. Chem. A 8 (2020) 3814–3821, https://doi.org/10.1039/c9ta12846h.
[26] J. Wang, S. Yin, M. Komatsu, Q. Zhang, F. Saito, T. Sato, Preparation and characterization of nitrogen doped SrTiO3 photocatalyst, J. Photochem. Photobiol. A: Chem. 165 (2004) 149–156, https://doi.org/10.1016/j.jphotochem.2004.02.022.
[27] S. Ouyang, H. Tong, N. Umezawa, J. Cao, P. Li, Y. Bi, Y. Zhang, J. Ye, Surface-alkalinization-induced enhancement of photocatalytic H2 evolution over SrTiO3-based photocatalysts, J. Am. Chem. Soc. 134 (2012) 1974–1977, https://doi.org/10.1021/ja210610h.
[28] S. Patial, V. Hasija, P. Raizada, P. Singh, A.A.P. Khan Singh, A.M. Asiri, Tunable photocatalytic activity of SrTiO3 for water splitting: strategies and future scenario, J. Environ. Chem. Eng. 8 (2020) 103791, https://doi.org/10.1016/j.jece.2020.103791.
[29] C.-H. Lee, N.J. Podraza, Y. Zhu, R.F. Berger, S. Shen, M. Sestak, R.W. Collins, L. F. Kourkoutis, J.A. Mundy, H. Wang, Q. Mao, X. Xi, L.J. Brillson, J.B. Neaton, D. A. Muller, D.G. Schlom, Effect of reduced dimensionality on the optical band gap of SrTiO3, Appl. Phys. Lett. 102 (2013) 122901, https://doi.org/10.1063/1.4798241.
[30] Y. Yamada, Y. Kanemitsu, Band-to-band photoluminescence in SrTiO3, Phys. Rev. B 82 (2010), https://doi.org/10.1103/PhysRevB.82.121103.
[31] X.G. Guo, X.S. Chen, Y.L. Sun, L.Z. Sun, X.H. Zhou, W. Lu, Electronic band structure of Nb doped SrTiO3 from first principles calculation, Phys. Lett. A 317 (2003) 501–506, https://doi.org/10.1016/j.physleta.2003.09.014.
[32] C. Wang, H. Qiu, T. Inoue, Q. Yao, Band gap engineering of SrTiO 3 for water splitting under visible light irradiation, Int. J. Hydrog. Energy 39 (2014) 12507–12514, https://doi.org/10.1016/j.ijhydene.2014.06.059.
[33] G. Wu, P. Li, D. Xu, B. Luo, Y. Hong, W. Shi, C. Liu, Hydrothermal synthesis and visible-light-driven photocatalytic degradation for tetracycline of Mn-doped SrTiO3 nanocubes, Appl. Surf. Sci. 333 (2015) 39–47, https://doi.org/10.1016/j.apsusc.2015.02.008.
[34] X. Yan, L. Constantin, Y. Lu, J.-F. Silvain, M. Nastasi, B. Cui, f 0.2 Zr 0.2 Ta 0.2 Nb 0.2 Ti 0.2)C high-entropy ceramics with low thermal conductivity, J. Am. Ceram. Soc. 101 ((H) (2018) 4486–4491, https://doi.org/10.1111/jace.15779.
[35] J. Zhou, J. Zhang, F. Zhang, B. Niu, L. Lei, W. Wang, High-entropy carbide: a novel class of multicomponent ceramics, Ceram. Int. 44 (2018) 22014–22018, https://doi.org/10.1016/j.ceramint.2018.08.100.
[36] N. Travitzky, A. Bonet, B. Dermeik, T. Fey, I. Filbert-Demut, L. Schlier, T. Schlordt, P. Greil, Additive manufacturing of ceramic-based materials, Adv. Eng. Mater. 16 (2014) 729–754, https://doi.org/10.1002/adem.201400097.
[37] O.H. Laguna, P.F. Lietor, F.I. Godino, F.A. Corpas-Iglesias, A review on additive manufacturing and materials for catalytic applications: milestones, key concepts, advances and perspectives, Mater. Des. 208 (2021) 109927, https://doi.org/10.1016/j.matdes.2021.109927.
[38] Z.C. Eckel, C. Zhou, J.H. Martin, A.J. Jacobsen, W.B. Carter, T.A. Schaedler, Additive manufacturing of polymer-derived ceramics, Science 351 (2016) 58–62, https://doi.org/10.1126/science.aad2688.
[39] Y. Lakhdar, C. Tuck, J. Binner, A. Terry, R. Goodridge, Additive manufacturing of advanced ceramic materials, Prog. Mater. Sci. 116 (2021) 100736, https://doi.org/10.1016/j.pmatsci.2020.100736.
[40] I. Cooperstein, E. Shukrun, O. Press, A. Kamyshny, S. Magdassi, Additive manufacturing of transparent silica glass from solutions, ACS Appl. Mater. Interfaces 10 (2018) 18879–18885, https://doi.org/10.1021/acsami.8b03766.
[41] M. Wang, C. Xie, R. He, G. Ding, K. Zhang, G. Wang, D. Fang, Polymer-derived silicon nitride ceramics by digital light processing based additive manufacturing, J. Am. Ceram. Soc. 102 (2019) 5117–5126, https://doi.org/10.1111/jace.16389.
[42] D.G. Moore, L. Barbera, K. Masania, A.R. Studart, Three-dimensional printing of multicomponent glasses using phase-separating resins, Nat. Mater. 19 (2020) 212–217, https://doi.org/10.1038/s41563-019-0525-y.
[43] S. Zakeri, M. Vippola, E. Levänen, A comprehensive review of the photopolymerization of ceramic resins used in stereolithography, Addit. Manuf. 35 (2020) 101177, https://doi.org/10.1016/j.addma.2020.101177.
[44] A. Ovsianikov, J. Viertl, B. Chichkov, M. Oubaha, B. MacCraith, I. Sakellari, A. Giakoumaki, D. Gray, M. Vamvakaki, M. Farsari, C. Fotakis, Ultra-low shrinkage hybrid photosensitive material for two-photon polymerization microfabrication, ACS Nano 2 (2008) 2257–2262, https://doi.org/10.1021/nn800451w.
[45] A. Vyatskikh, R.C. Ng, B. Edwards, R.M. Briggs, J.R. Greer, Additive Manufacturing of high-refractive-index, nanoarchitected titanium dioxide for 3d dielectric photonic crystals, Nano Lett. 20 (2020) 3513–3520, https://doi.org/10.1021/acs.nanolett.0c00454.
[46] F. Kamutzki, M.F. Bekheet, S. Schneider, A. Gurlo, D.A. Hanaor, A comparison of syntheses approaches towards functional polycrystalline silicate ceramics, Open Ceram. 9 (2022) 100241, https://doi.org/10.1016/j.oceram.2022.100241.
[47] H. Yang, S. Klemm, J. Müller, M.F. Bakheet, A. Gurlo, D.A. Hanaor, Synthesis of high-entropy carbides from multi-metal polymer precursors, J. Eur. Ceram. Soc. 43 (2023) 4233–4243, https://doi.org/10.1016/j.jeurceramsoc.2023.03.050.
[48] X. Wang, F. Schmidt, D. Hanaor, P.H. Kamm, S. Li, A. Gurlo, Additive manufacturing of ceramics from preceramic polymers: a versatile stereolithographic approach assisted by thiol-ene click chemistry, Addit. Manuf. 27 (2019) 80–90, https://doi.org/10.1016/j.addma.2019.02.012.
[49] J. Rodriguez-Carvajal, Recent developments of the program FULLPROF, in Commission on, Powder Diffr. (IUCr), Newsl. 26 (2001) 12–19 (https://doi.org/Powder).
[50] C. Schlesiger, L. Anklamm, H. Stiel, W. Malzer, B. Kanngießer, XAFS spectroscopy by an X-ray tube based spectrometer using a novel type of HOPG mosaic crystal and optimized image processing, J. Anal. At. Spectrom. 30 (2015) 1080–1085, https://doi.org/10.1039/C4JA00303A.
[51] C. Schlesiger, S. Praetz, R. Gnewkow, W. Malzer, B. Kanngießer, Recent progress in the performance of HAPG based laboratory EXAFS and XANES spectrometers, J. Anal. . Spectrom. 35 (2020) 2298–2304, https://doi.org/10.1039/D0JA00208A.
[52] B. Ravel, M. Newville, ATHENA, ARTEMIS, HEPHAESTUS: data analysis for X-ray absorption spectroscopy using IFEFFIT, J. Synchrotron Radiat. 12 (2005) 537–541, https://doi.org/10.1107/S0909049505012719.
[53] B.L. Mojet, S.D. Ebbesen, L. Lefferts, Light at the interface: the potential of attenuated total reflection infrared spectroscopy for understanding heterogeneous catalysis in water, Chem. Soc. Rev. 39 (2010) 4643–4655, https://doi.org/10.1039/C0CS00014K.
[54] M. Burgos, M. Langlet, The sol-gel transformation of TIPT coatings: a FTIR study, Thin Solid Films 349 (1999) 19–23, https://doi.org/10.1016/S0040-6090(99)00139-X.
[55] C. Yan, R. Liu, Y. Cao, C. Zhang, D. Zhang, Synthesis of submicrometer zirconium carbide formed from inorganic–organic hybrid precursor pyrolysis, J. Sol. -Gel Sci. Technol. 64 (2012) 251–256, https://doi.org/10.1007/s10971-012-2854-z.
[56] L. Feng, H. Yang, X. Dong, H. Lei, Di Chen, pH-sensitive polymeric particles as smart carriers for rebar inhibitors delivery in alkaline condition, J. Appl. Polym. Sci. 135 (2018) 45886, https://doi.org/10.1002/app.45886.
[57] M. Kourgiantakis, M. Matzapetakis, C.P. Raptopoulou, A. Terzis, A. Salifoglou, Lead–citrate chemistry. Synthesis, spectroscopic and structural studies of a novel lead(II)–citrate aqueous complex, Inorg. Chim. Acta 297 (2000) 134–138, https://doi.org/10.1016/S0020-1693(99)00339-4.
[58] X. Du, M. Zhou, S. Deng, Z. Du, X. Cheng, H. Wang, Poly(ethylene glycol)-grafted nanofibrillated cellulose/graphene hybrid aerogels supported phase change composites with superior energy storage capacity and solar-thermal conversion efficiency, Cellulose 27 (2020) 4679–4690, https://doi.org/10.1007/s10570-020-03110-z.
[59] N. Cao, Y. Zhao, H. Chen, J. Huang, M. Yu, Y. Bao, D. Wang, S. Cui, Poly(ethylene glycol) becomes a supra-polyelectrolyte by capturing hydronium ions in water, Macromolecules 55 (2022) 4656–4664, https://doi.org/10.1021/acs.macromol.2c00014.
[60] D.-M. Liu, Influence of porosity and pore size on the compressive strength of porous hydroxyapatite ceramic, Ceram. Int. 23 (1997) 135–139, https://doi.org/10.1016/S0272-8842(96)00009-0.
[61] H. Zhao, L. Li, S. Ding, C. Liu, J. Ai, Effect of porous structure and pore size on mechanical strength of 3D-printed comby scaffolds, Mater. Lett. 223 (2018) 21–24, https://doi.org/10.1016/j.matlet.2018.03.205.
[62] T. Luping, A study of the quantitative relationship between strength and pore-size distribution of porous materials, Cem. Concr. Res. 16 (1986) 87–96, https://doi.org/10.1016/0008-8846(86)90072-4.
[63] N.F. Muhamad, R.A. Maulat Osman, M.S. Idris, M.N. Mohd Yasin, Physical and electrical properties of SrTiO 3 and SrZrO 3, EPJ Web Conf. 162 (2017) 1052, https://doi.org/10.1051/epjconf/201716201052.
[64] A.K. Mandal, G. Panchal, S. Chowdhury, A. Jana, R.J. Choudhary, D.M. Phase, Electronic and magnetic properties of stoichiometric and off-stoichiometric SrMnO3 thin films, J. Supercond. Nov. Magn. 33 (2020) 1633–1636, https://doi.org/10.1007/s10948-019-05210-9.
[65] J. Bai, J. Yang, W. Dong, Y. Zhang, W. Bai, X. Tang, Structural and magnetic properties of perovskite SrMnO 3 thin films grown by molecular beam epitaxy, Thin Solid Films 644 (2017) 57–64, https://doi.org/10.1016/j.tsf.2017.08.052.
[66] Y. Su, S. Huang, T. Wang, L. Peng, X. Wang, Defect-meditated efficient catalytic activity toward p-nitrophenol reduction: A case study of nitrogen doped calcium niobate system, J. Hazard. Mater. 295 (2015) 119–126, https://doi.org/10.1016/j.jhazmat.2015.04.036.

[67] N. Bosio, A. Schaefer, H. Grönbeck, Can oxygen vacancies in ceria surfaces be measured by O1s photoemission spectroscopy, J. Phys. Condens. Matter 34 (2022), https://doi.org/10.1088/1361-648X/ac4f7b.
[68] M. Muralidharan, V. Anbarasu, A. Elaya Perumal, K. Sivakumar, Room temperature ferromagnetism in Cr doped SrSnO3 perovskite system, J. Mater. Sci: Mater. Electron 28 (2017) 4125–4137, https://doi.org/10.1007/s10854-016-6032-x.
[69] Z.H. Lim, K. Ahmadi-Majlan, E.D. Grimley, Y. Du, M. Bowden, R. Moghadam, J. M. LeBeau, S.A. Chambers, J.H. Ngai, Structural and electrical properties of single crystalline SrZrO3 epitaxially grown on Ge (001), J. Appl. Phys. 122 (2017) 084102, https://doi.org/10.1063/1.5000142.
[70] G. Xing, L. Zhao, T. Sun, Y. Su, X. Wang, Hydrothermal derived nitrogen doped SrTiO3 for efficient visible light driven photocatalytic reduction of chromium(VI), Springerplus 5 (2016) 1132, https://doi.org/10.1186/s40064-016-2804-2.
[71] Q. Tian, L. Zhang, J. Liu, N. Li, Q. Ma, J. Zhou, Y. Sun, Synthesis of MoS 2 /SrZrO 3 heterostructures and their photocatalytic H 2 evolution under UV irradiation, RSC Adv. 5 (2015) 734–739, https://doi.org/10.1039/C4RA11135D.
[72] M.D. McDaniel, C. Hu, S. Lu, T.Q. Ngo, A. Posadas, A. Jiang, D.J. Smith, E.T. Yu, A. A. Demkov, J.G. Ekerdt, Atomic layer deposition of crystalline SrHfO 3 directly on Ge (001) for high- k dielectric applications, J. Appl. Phys. 117 (2015) 54101, https://doi.org/10.1063/1.4906953.
[73] A. Karaphun, S. Hunpratub, T. Putjuso, E. Swatsitang, Characterization and dielectric properties of SrTi 1−x Mn x O 3 ceramics, Jpn. J. Appl. Phys. 54 (2015) 06FH09, https://doi.org/10.7567/JJAP.54.06FH09.
[74] R. Vali, Structural phases of SrHfO3, Solid State Commun. 148 (2008) 29–31, https://doi.org/10.1016/j.ssc.2008.07.018.
[75] M. Karmaoui, E.V. Ramana, D.M. Tobaldi, L. Lajaunie, M.P. Graça, R. Arenal, M. P. Seabra, J.A. Labrincha, R.C. Pullar, High dielectric constant and capacitance in ultrasmall (2.5 nm) SrHfO 3 perovskite nanoparticles produced in a low temperature non-aqueous sol–gel route, RSC Adv. 6 (2016) 51493–51502, https://doi.org/10.1039/c6ra06990h.
[76] A. Kumar, B. Khan, V. Yadav, A. Dixit, U. Kumar, M.K. Singh, Rietveld refinement, optical, dielectric and ac conductivity studies of Ba-doped SrSnO3, J. Mater. Sci: Mater. Electron 31 (2020) 16838–16848, https://doi.org/10.1007/s10854-020-04240-7.
[77] M. Glerup, K.S. Knight, F.W. Poulsen, High temperature structural phase transitions in SrSnO3 perovskite, Mater. Res. Bull. 40 (2005) 507–520, https://doi.org/10.1016/j.materresbull.2004.11.004.
[78] Y. Kumar, R. Kumar, R.J. Choudhary, A. Thakur, A.P. Singh, Reduction in the tilting of oxygen octahedron and its effect on bandgap with La doping in SrSnO3, Ceram. Int. 46 (2020) 17569–17576, https://doi.org/10.1016/j.ceramint.2020.04.056.
[79] F. Shi, K. Liang, Z.-M. Qi, Investigation of the crystal structure, lattice vibration and dielectric property of SrZrO 3 ceramic, J. Mater. Res. 31 (2016) 3249–3254, https://doi.org/10.1557/jmr.2016.340.